Above-Threshold Parameter Extraction and Modeling for Amorphous Silicon Thin-Film Transistors

Peyman Servati, *Student Member, IEEE*, Denis Striakhilev, *Member, IEEE*, and Arokia Nathan, *Senior Member, IEEE*

***Abstract*—This paper presents modeling and parameter extraction of the above-threshold characteristics of hydrogenated amorphorous silicon (*a*-Si:H) thin-film transistors (TFTs) in both linear and saturation regions of operation. A bias- and geometry-independent definition for field effect mobility considering the ratio of free-to-trapped carriers is introduced, which conveys the properties of the active semiconducting layer. A method for extraction of model parameters such as threshold voltage, effective mobility, band-tail slope, and contact resistance from the measurement results is presented. This not only provides insight to the device properties, which are highly fabrication-dependent, but also enables accurate and reliable TFT circuit simulation. The techniques presented here form the basis for extraction of physical parameters for other TFTs with similar gap properties, such as organic and polymer TFTs.**

***Index Terms*—Amorphous semiconductors, contact resistance, mobility, parameter extraction, thin-film transistors (TFTs), threshold voltage.**

I. Introduction

HYDROGENATED amorphous silicon (*a*-Si:H) thin-film transistors (TFTs) are extensively used as switching elements in active matrix liquid crystal displays (AMLCDs) and large-area matrix-addressed sensor arrays for imaging of optical and x-ray signals. Recently, new application areas have emerged, where the TFTs also serve as active circuit elements. Examples include the active matrix organic light-emitting diode (AMOLED) display [1] and the active pixel sensor (APS) [2]. For these applications, accurate TFT models and reliable methods for parameter extraction are critical for circuit design. Shur *et al*. [3]–[5], Leroux [6], Khakzar *et al*. [7], and other authors [8]–[13] have presented several models (e.g., AIM-SPICE [4]) for the different operational regimes of *a*-Si:H TFTs. Although the models predict the true terminal behavior of TFTs, the physical interpretation of the extracted parameters is somewhat limited. Knowledge of these parameters is vital for TFT device optimization. This signifies the importance of a model and associated extraction method that enables meaningful interpretation of extracted values. The extraction method may be more complex than methods currently used [14] by virtue of the departure from square law dependence of current–voltage (*I–V*) characteristics. The power parameter (α), if assumed two as in metal-oxide-semiconductor field-effect transistors (MOSFETs), can lead to inaccuracy. Cerdeira *et al*. [15] have included the effect of α in a unified extraction method, which we refer to as the integral method, based on the AIM-SPICE model. Here, an integral technique is used to extract α and threshold voltage (V_T) simultaneously. However, the effects of nonidealities such as contact resistance are not rigorously treated. These may vary by orders of magnitude due to process variations, thus strongly influencing the extracted values. Hence, they must be systematically investigated and identified.

In addition, the definition of parameters such as field effect mobility in TFTs, made from *a*-Si:H or other disordered semiconductors, is somewhat vague by virtue of both free and trapped carriers and their impact on device performance. This paper presents a simple and accurate definition of mobility considering free and trapped carriers, which lays the basis of a compact above-threshold model for *a*-Si:H TFTs. The parameter extraction method presented includes the effect of nonideal parameters such as contact resistance.

Section II revisits the conventional definition of field-effect mobility in *a*-Si:H TFTs. Based on the revised mobility definition, a compact above-threshold model and associated parameters is presented in Section III. Section IV describes measurement details for two TFT sets, along with the extraction of above-threshold parameters in Section V. Section VI presents a brief comparison of simulation and measurement results, and Section VII concludes the paper.

II. Field Effect Conductivity and Mobility in TFTs

The field effect mobility $(\mu_{\rm FET})$ in TFTs has been conventionally defined as a parameter, which relates the thin-film conductance at a location along the channel to the field-induced charge per unit area or

$$g = \mu_{\rm FET} Q_{\rm induced} = \mu_{\rm FET}(Q_{\rm free} + Q_{\rm trapped}). \quad (1)$$

Here, g is the channel conductance (Ω^{-1}), and $Q_{\rm induced}({\rm C/cm}^2)$ comprises of the charge trapped in the localized states $(Q_{\rm trapped})$ and the charge excited to the extended states $(Q_{\rm free})$ with a band mobility, $\mu_{\rm band}$. Thus, the field effect mobility may be approximated as the band mobility scaled by the ratio of the free charge to the total induced charge [5]

$$\mu_{\rm FET} = \mu_{\rm band}\frac{Q_{\rm free}}{Q_{\rm induced}} = \mu_{\rm band}\frac{Q_{\rm free}}{Q_{\rm free}+Q_{\rm trapped}}. \quad (2)$$

Manuscript received February 21, 2003; revised June 5, 2003. This work was supported in part by the Natural Sciences and Engineering Research Council of Canada (NSERC), by NSERC E.W.R. Steacie Fellowship, and by IGNIS Innovation Inc., Canada. The review of this paper was arranged by Editor C.-Y. Lu.

The authors are with the Electrical and Computer Engineering Department, University of Waterloo, Waterloo, ON N2L 3G1 Canada (e-mail: pservati@venus.uwaterloo.ca; dastriak@venus.uwaterloo.ca; anathan@venus.uwaterloo.ca).

Digital Object Identifier 10.1109/TED.2003.818156

Since the charge components ($Q_{\rm trapped}$ and $Q_{\rm free}$) represent the charge over the thickness of the thin film [3], [5], $\mu_{\rm FET}$ is representative of the variation or modulation of device conductance, and dependent on the geometry of the semiconductor and insulator layers and the channel charge profile.

Using (2) as the basic definition for field effect mobility, Shur *et al.* [4] present the above-threshold current equations of *a*-Si:H TFTs (for both linear and saturation regions) as a function of gate-source ($V_{\rm GS}$) and drain-source ($V_{\rm DS}$) voltages as

$$I_{\rm DS}=\begin{cases}\mu_{\rm FET}C_i\frac{W}{L}\\ \quad\times\left(V_{\rm GS}-V_T-\frac{V_{\rm DS}}{2\alpha_{\rm sat}}\right)V_{\rm DS} & V_{\rm DS}<\alpha_{\rm sat}(V_{\rm GS}-V_T)\\ \mu_{\rm FET}C_i\frac{W}{L}\\ \quad\times(V_{\rm GS}-V_T)^2\frac{\alpha_{\rm sat}}{2} & V_{\rm DS}\geq\alpha_{\rm sat}(V_{\rm GS}-V_T)\end{cases}. \tag{3}$$

Here, V_T denotes the threshold voltage, W the width, L the channel length, C_i the gate capacitance, and $\alpha_{\rm sat}$ a saturation parameter. Because of (2), $\mu_{\rm FET}$ becomes gate bias dependent and reduces to the following simple form [3]:

$$\mu_{\rm FET}=\mu_{\rm band}\left(\frac{V_{\rm GS}-V_T}{V_{AA}}\right)^{\gamma}. \tag{4}$$

Here, γ is a power parameter and V_{AA} the characteristic voltage for field-effect mobility. The voltage dependence in $\mu_{\rm FET}$ leads to a power-law dependence of $I_{\rm DS}-V_{\rm GS}$, with exponents $\gamma+1$ and $\gamma+2$ for the linear and saturation regions, respectively. Also, the conductance-based definition of $\mu_{\rm FET}$ leads to the geometry dependence, which is hidden in V_{AA}.

While (3) and (4) are simple and preserve the true character of the TFTs terminal behavior, they are heuristic in nature and somewhat undermine the physical interpretation of the extracted parameters. In the following, another presentation of mobility is discussed, which brings more insight to the properties of the active semiconducting layer. Fig. 1 shows the typical density of states (DOS) in the *a*-Si:H mobility gap [5]. The localized states in the gap may be approximated by the exponential distribution of the tail and deep states for both acceptor-like and donor-like states. States with energies higher than E_C (the mobility edge) are the extended states of the conduction band for which the electron band mobility, i.e., $\mu_{\rm band}$, holds true. Neglecting the hopping conduction for the localized states, the conductivity $\sigma_n(\Omega^{-1}{\rm cm}^{-1})$ is mainly due to the electrons excited to the extended states and can be written as

$$\sigma_n=q\mu_{\rm band}n_{\rm free}. \tag{5}$$

The density of free electrons $n_{\rm free}({\rm cm}^{-3})$ in the *a*-Si:H bulk is

$$n_{\rm free}=N_C\exp\left[\frac{(E_F-E_C)}{kT}\right]=N_{fi}\exp\left(\frac{\psi}{V_{th}}\right) \tag{6}$$

where E_F denotes the Fermi-level, N_C the concentration of free electrons when $E_F=E_C$, k the Boltzmanns constant, T the temperature, q the elementary charge, and V_{th} the thermal voltage ($=kT/q$). Here, $\psi=(E_F-E_i)/q$, and N_{fi} is defined as $N_C\exp[(E_i-E_C)/kT]$, where E_i is the intrinsic Fermi-level of *a*-Si:H (see Fig. 1). The band mobility $\mu_{\rm band}$ is dependent on the disorder of *a*-Si:H and expected to be ~ 13 cm^2/Vs at $T=300$ K [16].

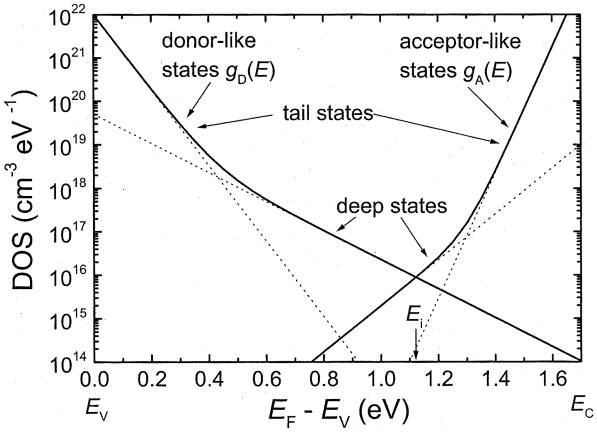

Fig. 1. Illustration of the DOS in intrinsic *a*-Si:H.

In the above-threshold region, the Fermi-level resides in the conduction band tail and, thus, the density of electrons trapped in the acceptor-like tail states prevails over other charge components ($n\sim n_{\rm trapped}$) [5], [17]. Similar to the formalism used by Shaw *et al.* [18], integrating over the exponential DOS weighted by the Fermi–Dirac function for the probability of an electron to occupy a state, the density of electrons trapped in the conduction band tail can be written as

$$n_{\rm trapped}=N_{ti}\exp\left(\frac{\psi}{V_{nt}}\right). \tag{7}$$

Here, V_{nt} is the characteristic slope of the conduction band tail, and N_{ti} the associated density of trapped electrons when $E_F=E_i$, respectively. These parameters may be obtained from the DOS and are temperature dependent due to the expansion of the Fermi–Dirac distribution as temperature increases.

Equations(6) and (7) yield a relation for the free electrons in terms of the trapped electrons (irrespective of ψ) as

$$n_{\rm free}=\frac{N_{fi}}{N_{ti}^{\frac{\alpha}{2}}}n_{\rm trapped}^{\frac{\alpha}{2}} \tag{8}$$

where $\alpha=2V_{nt}/V_{th}$. Using (5) and the above-threshold approximation ($n\sim n_{\rm trapped}$), the conductivity may be written as

$$\sigma_n=q\mu_{\rm band}n_{\rm free}=q\mu_{\rm band}\frac{N_{fi}}{N_{ti}^{\frac{\alpha}{2}}}n^{\frac{\alpha}{2}}. \tag{9}$$

In contrast to crystalline semiconductors, the conductivity is a nonlinear function of the field-induced charge. Equation (9) is a characteristic equation that describes the conductivity-charge relationship with no Fermi-level dependence. Thus, an effective mobility for a disordered material system with exponential DOS may be defined when the density of the induced charge is equal to a constant reference concentration N_0, viz.,

$$\mu_{\rm eff}=\frac{\sigma_n}{qN_0}=\mu_{\rm band}\frac{N_{fi}}{N_{ti}^{\frac{\alpha}{2}}}N_0^{\frac{\alpha}{2}-1}. \tag{10}$$

Where the electron concentration differs from N_0, the conductivity is modulated as $\sigma_n=q\mu_{\rm eff}n^{\alpha/2}/N_0^{\alpha/2-1}$ in accordance to (9) and (10). Here, the arbitrary constant N_0 is assumed to be 10^{17} cm^{-3}, which is of the order of the field induced charge density close to the interface in typical device operation when the

gate voltage is ten volts. This definition for mobility provides a bias- and geometry-independent measure for conduction.

III. Above-Threshold Compact Model

Based on the above definition of mobility, we model the *I–V* characteristics of *a*-Si:H TFTs [9]. The models are implemented in VerilogA hardware description language, which comes as a standard feature in most circuit simulation environments.

Fig. 2 illustrates the equivalent circuit model of the TFT in which the voltage-controlled current source $I_{\rm DS}$ represents the different regimes of operation such as above-threshold, subthreshold, and Poole–Frenkel [9]. The other current sources and capacitances are responsible for the transient response of the TFT and are described elsewhere [9]. The primed voltages $V'_{\rm GS}$ and $V'_{\rm DS}$ (see Fig. 2) control the current source $I_{\rm DS}$, thereby including the effect of source and drain contact resistances R_S and R_D [19], as

$$V'_{\rm GS} = V_{\rm GS} - I_{\rm DS}R_S \text{ and } V'_{\rm DS} = V_{\rm DS} - I_{\rm DS}(R_S + R_D) \quad (11)$$

respectively. The drain-source current as a function of gate-source ($V'_{\rm GS}$) and gate-drain ($V'_{\rm GD}$) voltages, in accordance to (37) derived in the Appendix, can be written as

$$I_{\rm DS} = \frac{\mu_{\rm eff}}{\alpha}\zeta C_i^{\alpha-1}\frac{W}{L_{\rm eff}}\left[(V'_{\rm GS}-V_T)^{\alpha} - (V'_{\rm GD}-V_T)^{\alpha}\right]. \quad (12)$$

Here, $\mu_{\rm eff}$ is the effective mobility, ζ the unit matching parameter (see Appendix), and $L_{\rm eff}$ the effective channel length. The equation for the linear region is derived using Taylors expansion of (12) (where $V'_{\rm GD}$ is substituted by $V'_{\rm GS} - V'_{\rm DS}$ and $V'_{\rm DS} \ll V'_{\rm GS}$) as

$$I_{\rm DS,lin} = \mu_{\rm eff}\zeta C_i^{\alpha-1}\frac{W}{L_{\rm eff}}(V'_{\rm GS}-V_T)^{\alpha-1}V'_{\rm DS}. \quad (13)$$

Substituting (11) into (13) yields

$$I_{\rm DS,lin} = \mu_{\rm eff}\zeta C_i^{\alpha-1}\frac{W}{L_{\rm eff}} \times (V_{\rm GS}-V_T-0.5V_{\rm DS})^{\alpha-1}(V_{\rm DS}-R_{\rm DS}I_{\rm DS}) \quad (14)$$

for the symmetric case where $R_D = R_S = R_{\rm DS}/2$.

For $V'_{\rm DS}$ voltages higher than the saturation voltage $V'_{\rm dsat}$, the TFT operates in the saturation region. The saturation voltage $V'_{\rm dsat}$ is the voltage at the internal drain node for which the density of mobile electrons at the drain side of the channel reduces to zero ("pinch-off" condition) and is given by

$$V'_{\rm dsat} = \alpha_{\rm sat}(V'_{\rm GS}-V_T) \quad (15)$$

where $\alpha_{\rm sat}$ is the saturation parameter. Substituting $V'_{\rm GS} - V'_{\rm dsat}$ for $V'_{\rm GD}$ in (12) yields

$$I_{\rm DS} = \frac{\mu_{\rm eff}}{\alpha}\zeta C_i^{\alpha-1}\frac{W}{L_{\rm eff}}\gamma_{\rm sat}(V'_{\rm GS}-V_T)^{\alpha} \quad (16)$$

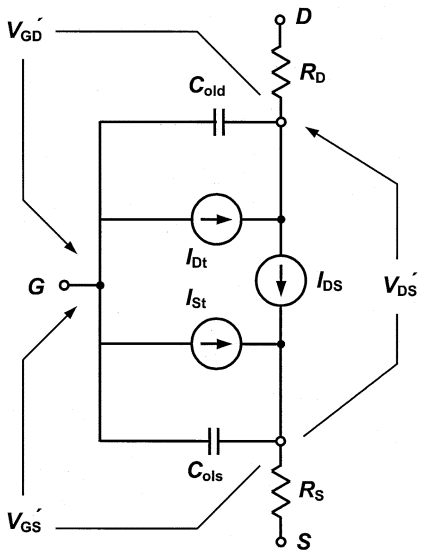

Fig. 2. Equivalent circuit of the compact TFT model.

where

$$\gamma_{\rm sat} = 1 - (1-\alpha_{\rm sat})^{\alpha}. \quad (17)$$

Substituting (11) into (16) and including the channel length modulation coefficient, x_{cm}, we have

$$I_{\rm DS} = \frac{\mu_{\rm eff}}{\alpha}\zeta C_i^{\alpha-1}\frac{W}{L_{\rm eff}}\gamma_{\rm sat}\left(V_{\rm GS} - \frac{R_{\rm DS}}{2}I_{\rm DS} - V_T\right)^{\alpha}x_{\rm cm}. \quad (18)$$

Here, $x_{cm} = 1 + \lambda V_{\rm DS}/L_{\rm eff}$, where λ is the channel length modulation parameter.

Observe that the power parameter (α) in (13) and (16) provide equivalent $I_{\rm DS} - V_{\rm GS}$ dependence as (3) with $\alpha = \gamma + 2$. However, C_i has a different power dependence and this is due to the dependence of V_{AA} on the gate insulator thickness, which stems from the conductance-based definition of field effect mobility in (3).

IV. Experimental

Fig. 3(a) shows the cross section of the TFT. The thicknesses of the different layers are summarized in Table1. The TFTs are fabricated using a standard trilayer process [20]. Fig. 3(b) depicts a photomicrograph of the fabricated TFTs with $W \sim 100\ \mu$m and different channel lengths, i.e., $L \sim 23, 33, 50, 80,$ and 130 μm, used in this study. A Keithley 4200 semiconductor characterization system is used for measurement of *I–V* characteristics. Here, delays of up to 20 s are used to deal with transient current fluctuations.

Two sets of TFTs are considered, which have completely distinct characteristics by virtue of the different process conditions for the *a*-Si:H and n^+ *a*-Si:H contact layers. TFT set I is representative of high mobility and low contact resistance. TFT set II is the opposite with lower mobility and high contact resistance. Details of the process conditions used have been reported elsewhere [21].

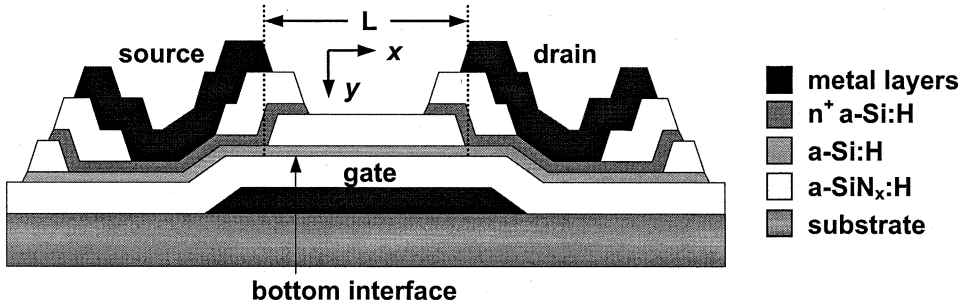

(a)

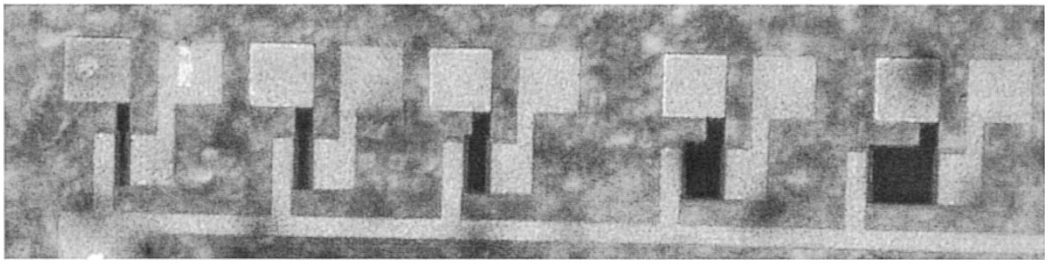

(b)

Fig. 3. (a) Cross section of the TFT structure showing its different layers. (b) Photomicrograph of TFTs with different channel length in TFT set II ($W \sim 100\,\mu$m and $L \sim 23, 33, 50, 80$, and $130\,\mu$m).

V. Parameter Extraction

A. Power Parameter (α), Threshold Voltage, and Contact Resistance

Based on the integral method, the linear region ($V_{\rm DS} = 50-100$ mV) may be used to extract parameters such as V_T and $\mu_{\rm eff}$ for a-Si:H TFTs. As opposed to the method used for MOSFETs [19], [22], the power parameter (α) needs to be extracted as well. Presence of a high contact resistance makes the extraction even more cumbersome. Fig. 4 illustrates simulation results for the linear $I_{\rm DS}-V_{\rm GS}$ characteristics of a TFT with aspect ratio of $100\,\mu$m$/23\,\mu$m, $\alpha = 2.34, V_T = 3$ V, and $\mu_{\rm eff} = 0.34$ cm^2/Vs, for different values of contact resistance ($R_{\rm DS}W$, the contact resistance for a unit width TFT). The in-set shows the extracted α and V_T using the integral method, highlighting the error in extracted values for $R_{\rm DS}W > 0.5\,{\rm k}\Omega-$cm. Unfortunately, this is a common range for the contact resistance in a-Si:H TFTs [14]. Therefore, to extract α and V_T more accurately we should eliminate the contact resistance induced error.

Fig. 5 compares the measured resistance between drain and source terminals ($R_m = V_{\rm DS}/I_{\rm DS,lin}$) for a long channel TFT ($L_{\rm max} = 200\,\mu$m) and that for a small channel TFT ($L_{\rm min} = 23\,\mu$m). The measured resistance for the former is scaled by the ratio of channel lengths, $k = L_{\rm min}/L_{\rm max} (= 23/200)$, which is the expected ratio for the resistances. In small channel TFTs, the contact resistance is the dominant part of the measured resistance, whereas, for the long channel case, e.g., $L > 200\,\mu$m, the channel resistance prevails. Based on (14), the difference between the two curves (see dotted curve in Fig. 5) approaches $R_{\rm DS}(1-k)$ at high $V_{\rm GS}$. This can be used to determine an estimate for $R_{\rm DS}$.

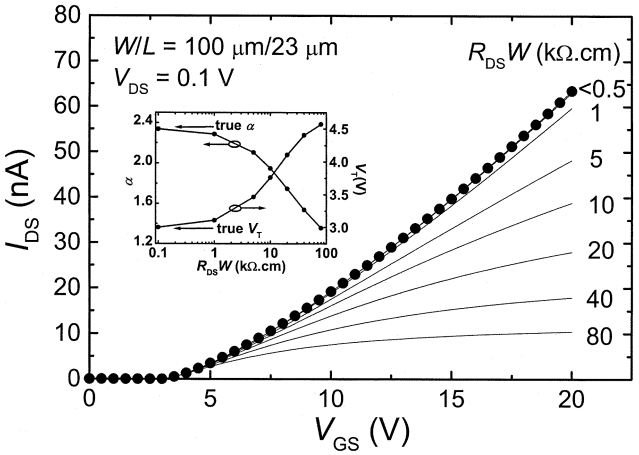

Fig. 4. Simulation results for linear transfer characteristics of a TFT with aspect ratio of $100\,\mu$m$/23\,\mu$m, $\alpha = 2.34$, $V_T = 3$ V, and $\mu_{\rm eff} = 0.34$ cm^2/Vs, plotted for different values of contact resistance ($R_{\rm DS}W$). Inset shows the extracted values of α and V_T using the integral method.

Having estimated $R_{\rm DS}$, we now proceed to find α and V_T. From (14) and (18), we have

$$\frac{I_{\rm DS,lin}}{g_{\rm mlin}} = \frac{V_{\rm GS}-V_T-0.5V_{\rm DS}}{\alpha-1}\frac{V_{\rm DS}}{V_{\rm DS}-R_{\rm DS}I_{\rm DS,lin}} \quad \text{and}$$
$$\frac{I_{\rm DS,sat}}{g_{\rm msat}} = \frac{V_{\rm GS}-V_T+R_{\rm DS}I_{\rm DS,sat}\frac{(\alpha-1)}{2}}{\alpha} \tag{19}$$

where parameters $g_{\rm mlin}$ and $g_{\rm msat}$ are defined as

$$g_{\rm mlin} \equiv \frac{\partial I_{\rm DS,lin}}{\partial V_{\rm GS}} \quad \text{and} \quad g_{\rm msat} \equiv \frac{\partial I_{\rm DS,sat}}{\partial V_{\rm GS}} \tag{20}$$

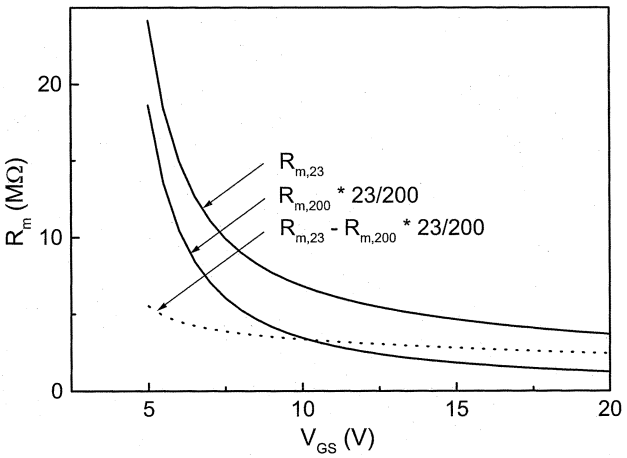

Fig. 5. Measured resistance for TFTs with channel length $L = 200\ \mu$m and $L = 23\ \mu$m of set II.

respectively. The left-handsides of (19) may be determined from the data obtained in the linear and saturation regions. Assuming the contact resistance related terms are negligible in (19) (i.e., $R_{\rm DS}I_{\rm DS,lin} \ll V_{\rm DS}$ and $R_{\rm DS}I_{\rm DS,sat} \ll V_{\rm GS} - V_T$ for linear and saturation regions, respectively), we may write

$$\frac{I_{\rm DS,lin}}{g_{\rm mlin}} = \frac{V_{\rm GS} - V_T - 0.5V_{\rm DS}}{\alpha - 1} \text{ and } \frac{I_{\rm DS,sat}}{g_{\rm msat}} = \frac{V_{\rm GS} - V_T}{\alpha}. \tag{21}$$

Thus, for the low contact resistance case ($R_{\rm DS}W < 0.5\ \text{k}\Omega - \text{cm}$), a plot of $I_{\rm DS,lin}/g_{\rm mlin}$ or $I_{\rm DS,sat}/g_{\rm msat}$ versus $V_{\rm GS}$ must be a straight line whose slope and intercept on the abscissa yield α and V_T, respectively. This is similar to the result of the integral method [15]. However, for the high contact resistance case ($R_{\rm DS}W > 0.5\ \text{k}\Omega - \text{cm}$), the value of α extracted using (21) has a significant error, which must be eliminated using the modified versions of $I_{\rm DS,lin}/g_{\rm mlin}$ or $I_{\rm DS,sat}/g_{\rm msat}$ as a function of $V_{\rm GS}$ [23]. Alternatively, we can find the expected error in α from the estimated value of $R_{\rm DS}$. According to (19), the contact resistance induced error in the value of α ($\Delta\alpha_{\rm lin}$ and $\Delta\alpha_{\rm sat}$) extracted from the best fit to $I_{\rm DS,lin}/g_{\rm mlin}$ or $I_{\rm DS,sat}/g_{\rm msat}$ versus $V_{\rm GS}$ curves in the range $(V_T + 1, V_{\rm GS0})$ may be estimated as

$$\Delta\alpha_{\rm lin} \approx -k_0(\alpha - 1) \quad \text{and} \quad \Delta\alpha_{\rm sat} \approx -\frac{k_0}{2}(\alpha - 1) \tag{22}$$

respectively, where

$$k_0 = \frac{R_{\rm DS}W\mu_{\rm eff}\zeta C_i^{\alpha-1}}{L_{\rm eff}(V_{\rm GS0} - V_T)^{\alpha-1}}. \tag{23}$$

Therefore, adding $k_0(\alpha - 1)$ and $k_0(\alpha - 1)/2$ to the extracted value of α from linear and saturation data, respectively, should compensate for the contact resistance effects. Note that the data from saturation region is less sensitive to contact resistance effects. In addition, it can be shown that $k_0 \sim R_{\rm DS}/R_m$. Thus, the data measured for the maximum channel length TFT, which has the highest R_m, should be used to reduce the error significantly. In addition, since increasing $V_{\rm GS0}$ increases k_0, $V_{\rm GS0}$ should be determined in a manner such that $R_{\rm DS} \ll R_m$ so as to achieve minimal contact resistance induced error. Based on the extracted value of α, V_T can be extracted for TFTs with different channel length using the best fit to the $I_{\rm DS}^{1/(\alpha-1)}$ versus $V_{\rm GS}$ graph at small currents, where the contact resistance induced error is trivial.

Having extracted α and V_T, we can find a more accurate value for contact resistance using the measurement results for TFTs with different channel lengths. Here, the channel length $L_{\rm eff}$ is the value that provides good agreement between theory and experiment. Similar to MOSFETs [22], [24], $L_{\rm eff}$ may differ from the mask-defined and physical channel length L due to channel enlargement at the edge of the source and the drain contacts. From (14), the measured resistance of a TFT with unit width (R_mW) can be written as

$$R_mW = \frac{V_{\rm DS}}{I_{\rm DS}}W = R_{\rm DS}W + \frac{L + \Delta L}{\mu_{\rm eff}\zeta C_i^{\alpha-1}(V_{\rm GS} - V_T)^{\alpha-1}}, \tag{24}$$

where $L + \Delta L$ is substituted for $L_{\rm eff}$. According to (24), R_mW versus L curves plotted for different values of $V_{\rm GS}$ should have an intercept point with coordinates ΔL and $R_{\rm DS}W$ [14], [27]. Fig. 6 shows this plot and the intercept point for the TFTs in set I. Note that since each transistor has an identical V_T, the measured data must be corrected to have a constant applied voltage ($V_{\rm GS} - V_T$) for each curve.

To determine the intercept point (ΔL, $R_{\rm DS}W$) more accurately [28], (24) is rewritten as

$$R_mW = AL + B \tag{25}$$

where

$$A = \frac{1}{\mu_{\rm eff}\zeta C_i^{\alpha-1}(V_{\rm GS} - V_T)^{\alpha-1}} \text{ and } B = R_{\rm DS}W + A\Delta L. \tag{26}$$

Equation (26) indicates that a plot of B as a function of A is a line with $R_{\rm DS}W$ and ΔL as the ordinate intercept point and the slope, respectively. Fig. 7 illustrates this (B versus A) plot for both TFT sets. As can be seen, the extracted $R_{\rm DS}W$ (see Table II) value for the TFT set II is approximately two orders of magnitude higher than that of set I.

The accuracy of the extracted values for $R_{\rm DS}W, \Delta L, V_T$, and α may be further improved through an iterative process.

B. Effective Mobility

A plot of $A^{-1/(\alpha-1)}$ versus $V_{\rm GS} - V_T$ may be used to extract the effective mobility since the impact of contact resistance, power parameter, and threshold voltage variation is included in A. This contact resistance included (CRI) mobility plot (see Fig. 8) is similar to the $(I_{\rm DS}/W)^{1/2}$ versus $V_{\rm GS}$ curve used to extract mobility in MOSFETs. The slope (s) of the best fit to the CRI curve may be used to find $\mu_{\rm eff}$ as

$$\mu_{\rm eff} = \frac{1}{\zeta}\left(\frac{s}{C_i}\right)^{\alpha-1}. \tag{27}$$

C. Saturation Parameters

For extraction of $\gamma_{\rm sat}$ (or $\alpha_{\rm sat}$), the measurement data in saturation region ($V_{\rm DS} = V_{\rm GS}$ or $V_{\rm DS} = 20$ V) for the TFT with maximum channel length ($L \sim 200\ \mu$m) is used so as to minimize contact resistance effects. Based on (18), the slope S of

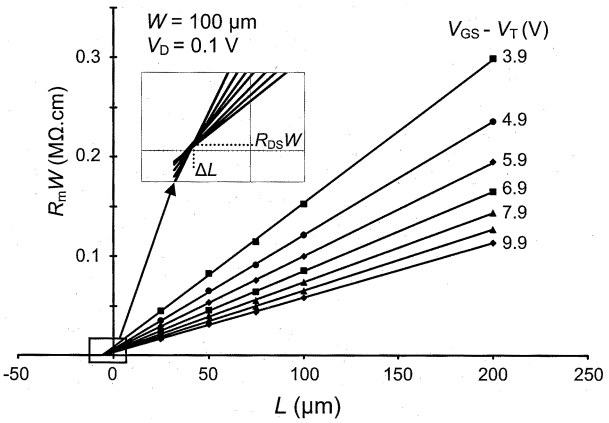

Fig. 6. R_mW of TFT set I as a function of channel length L for different values of the applied voltage $V_{\rm GS}-V_T$ used for extraction of $R_{\rm DS}W$ and ΔL.

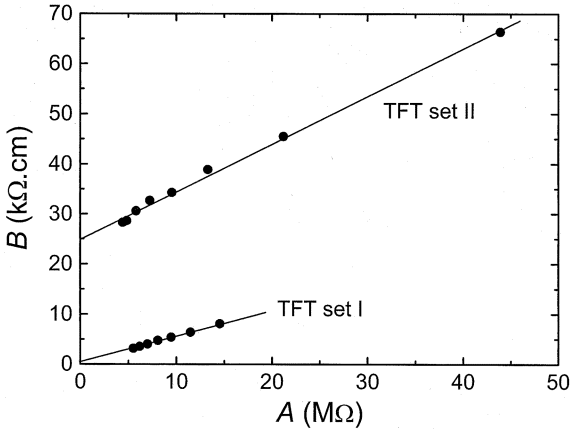

Fig. 7. B as a function of A for both TFT sets.

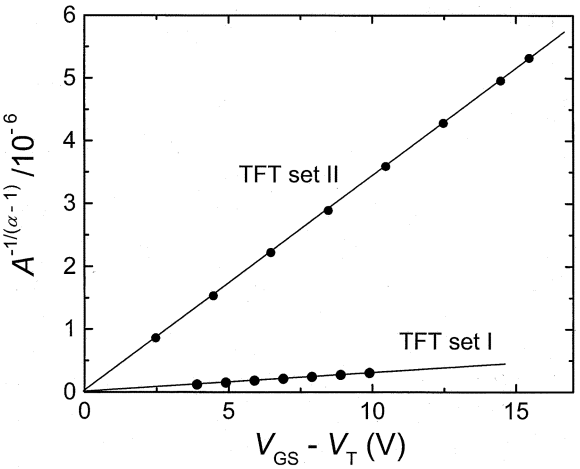

Fig. 8. $A^{-1/(\alpha-1)}$ versus $V_{\rm GS}-V_T$ (CRI mobility plot) for both TFT sets.

the best fit to the $(I_{\rm DS}L_{\rm eff}/W)^{1/\alpha}$ versus $V_{\rm GS}$ curve for the long channel TFT yields $\gamma_{\rm sat}$ as

$$\gamma_{\rm sat}=\frac{\alpha S^{\alpha}}{\mu_{\rm eff}\zeta C_i^{\alpha-1}x_{\rm cm}}. \tag{28}$$

Then, $\alpha_{\rm sat}$ may be found from (17).

Since the channel length modulation effect reduces with increasing channel length, it is more accurate to extract λ from the output characteristics ($I_{\rm DS}$ versus $V_{\rm DS}$) of the TFT with minimum channel length ($L\sim 23\ \mu$m). Here, $\lambda=L_{\rm eff}/V_A$, where V_A is the Early voltage and is defined in the usual sense as the absolute value of the intercept on the $V_{\rm DS}$ axis.

TABLE I
THICKNESS OF THE DIFFERENT LAYERS OF THE TFT STRUCTURE

Layer	Thickness (nm)
Gate metal	130
a-SiN$_x$:H gate dielectric	300
a-Si:H	50
a-SiN$_x$:H passivation layer	250
n^+a-Si:H contact layer	50
Al metallization layer	500

VI. DISCUSSION

Using the parameter extraction method described in the previous section, the model parameters for the above-threshold characteristics of a-Si:H TFTs are extracted for both TFT sets, and are summarized in Table II, which include both physical ($\mu_{\rm eff}$, V_T, α, $R_{\rm DS}W$, and ΔL) and dependent or fitting (ζ, V_{nt}, $\alpha_{\rm sat}(\gamma_{\rm sat})$, and λ) parameters. Fig. 9 and Fig. 10 illustrate a comparison of simulation and measurement results for the linear transfer characteristics of TFTs in sets I and II, respectively. Figs. 11 and 12 show a comparison between simulation and measurement results for the *I–V* characteristics of the TFT with channel length $L\sim 23\ \mu$m in set I and II, respectively. As can be seen, good agreement between modeling and experimental results is obtained with a discrepancy less than 5%.

The extracted values of α (see Table II) reflect the distribution of states in the conduction band tail following the relationship, $\alpha=2V_{nt}/V_{th}$. According to the values presented in Table II, the slopes of the conduction band tail for TFTs in set I and II are 26.2 and 29.3 meV, respectively. The higher value of V_{nt} for TFTs in set II indicates a slower decrease in the density of tail states as we move toward the middle of the gap from the mobility edge, which corroborates with the lower effective mobility extracted for this set [17]. The impact of α (or V_{nt}) on $\mu_{\rm eff}$, which is a measure for dispersive conduction in a-Si:H, becomes apparent if we recast (10) in the following form:

$$\mu_{\rm eff}=\mu_{\rm band}\frac{N_C}{N_0}\left(\frac{N_0}{N_{tC}}\right)^{\frac{\alpha}{2}} \tag{29}$$

where $N_{tC}=n_{\rm trapped}$ at $E_F=E_C$. Assuming $N_C=10^{19}$ cm^{-3} and $\mu_{\rm band}=13$ cm^2/Vs, the value of N_{tC} is retrieved as $\sim 10^{20}$ cm^{-3} from the extracted values of effective mobility for both sets. Thus, in (29), the effective mobility decreases if α increases, since $N_0/N_{tC}\sim 10^{-3}$. This indicates that the DOS starts from approximately the same value at the conduction band edge and decays with different slopes resulting in different $\mu_{\rm eff}$.

It is also interesting to note that the TFTs in set I had a total mask overlap length of $\sim 5\ \mu$m, which appears to correlate with the value of $\Delta L=5.42\ \mu$m extracted in this study. However,

TABLE II
EXTRACTED PARAMETERS FOR BOTH TFT SETS

Physical Parameters	TFT set I	TFT set II	Unit
μ_{eff} – effective mobility	0.938	0.497	cm^2/Vs
V_T – threshold voltage ($L \sim 200\ \mu m$)	3.9	3.0	V
α – power parameter	2.035	2.270	-
$R_{DS}W$ – contact resistance	0.229	25.0	kΩ-cm
ΔL – channel length enlargement	5.42	9.52	μm
Dependent or Fitting Parameters	**TFT set I**	**TFT set II**	**Unit**
ζ – unit matching parameter	1.77	84.2	$(C/cm^2)^{\alpha-2}$
V_{nt} – conduction band tail slope	26.2	29.3	mV
α_{sat} – saturation parameter	0.9434	0.7937	-
γ_{sat} – saturation current parameter	0.9971	0.9722	-
λ – channel length modulation parameter	0.611	1.18	$\mu m/V$

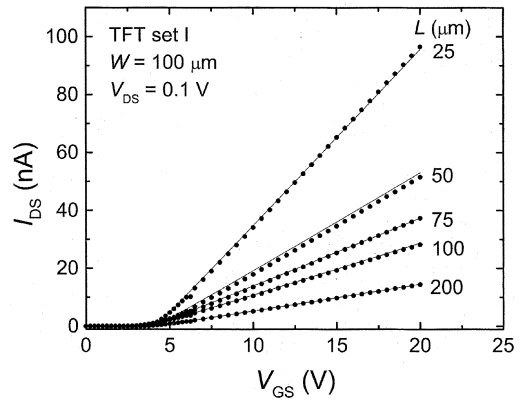

Fig. 9. Comparison between model simulation results (solid lines) and measurement data (circles) for the linear transfer characteristics of TFTs in set I.

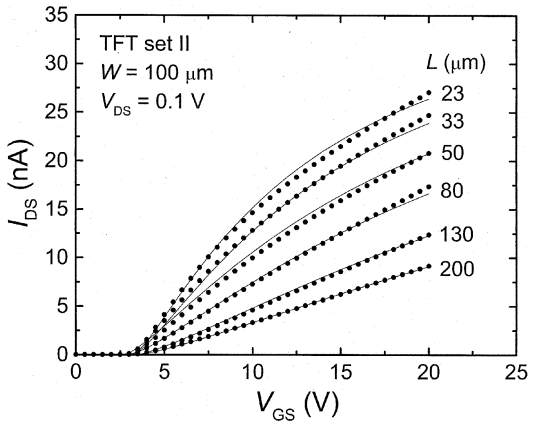

Fig. 10. Comparison between model simulation results (solid lines) and measurement data (circles) for the linear transfer characteristics of TFTs for set II.

for the TFTs in set II (with mask overlap length of $\sim 5\ \mu m$), the extracted ΔL is $\sim 9\ \mu m$. This is possibly due to the expansion of channel by virtue of the highly resistive contact layer [27].

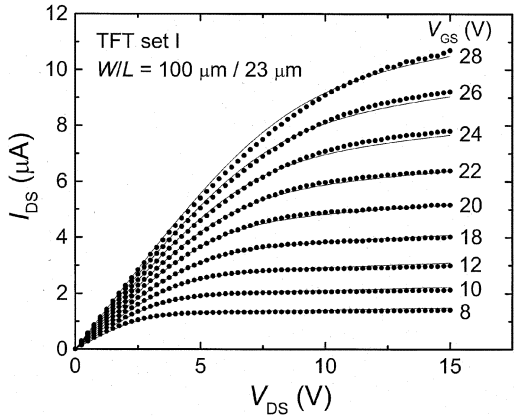

Fig. 11. Comparison between model simulation results (solid lines) and measurement data (circles) for the output *I–V* characteristics of the TFT with $L \sim= 23\ \mu m$ in set I.

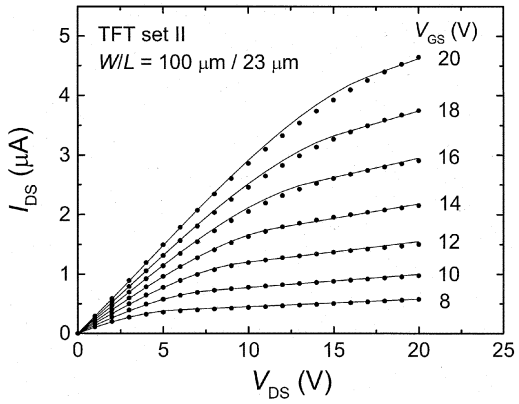

Fig. 12. Comparison between model simulation results (solid lines) and measurement data (circles) for the output *I–V* characteristics of the TFT with $L \sim= 23\ \mu m$ in set II.

Thus, a specific contact resistance $(R_{\rm con})$ associated with the source and drain overlap areas may be defined as

$$R_{\rm con} = \frac{R_{\rm DS}W}{2}\Delta L\ \Omega - {\rm cm}^2 \tag{30}$$

for an overall measure of contact quality [27].

VII. Conclusion

The quest for new materials and process conditions for improved TFT performance coupled with newly emerging technologies such as organic TFTs demands meaningful models and associated characterization parameters that relate device characteristics to material properties. While the parameter set needs to convey pertinent physical properties of the bulk and interfaces, it should be compact and amenable to expedient simulation of TFT circuits. This paper presented a minimal set of such parameters for description of the above-threshold characteristics of a-Si:H TFTs, along with associated parameter extraction techniques. A new effective mobility, $\mu_{\rm eff}$ as defined by (29), has been developed considering trapped and free carriers to provide a description of the field-effect conductance from measurement results of terminal behavior. Here, the power parameter α, which is a measure for the density of conduction band tail states and characterizes dispersive conduction in disordered materials, has a direct bearing on the value of $\mu_{\rm eff}$. As with the effective mobility case, the characterization parameters of TFTs depart from those of crystalline field-effect transistors due to the distinct effects of material disorder. In addition, nonidealities such as contact resistance must be systematically examined, since they can vary by orders of magnitude due to process variations, thus strongly influencing the extracted values. Good agreement between modeling and experimental results is obtained with a discrepancy of less than 5%.

Appendix

For convenience, we adopt a change in notation for the trapped charge in the conduction band tail from $n_{\rm trapped}$ to n_t. Assuming n_t as the main charge component in the above-threshold region, the one-dimensional Poissons equation may be written as

$$\frac{\partial E_y}{\partial y} = -\frac{q}{\varepsilon} n_t(\psi) \quad \text{and} \quad E_y = -\frac{\partial \psi}{\partial y}. \tag{31}$$

Here, E_y is the electric field perpendicular to the a-Si:H surface, ε the a-Si:H dielectric constant, and y the location across the a-Si:H layer [see Fig. 3(a)]. Solving (31) for the electric field, using the exponential distribution of trapped electrons defined by (7), yields

$$E_y = -\sqrt{\frac{q\alpha V_{th} n_t(\psi)}{\varepsilon}} \tag{32}$$

for the simplified boundary conditions, $E_0 = 0$ and $\psi_0 = 0$ in the a-Si:H bulk far from the front interface. Gauss' Law for the electric field E_s at the a-Si:H interface yields, $\varepsilon E_s = -C_i V_i$, where V_i is the drop in electric potential over the gate dielectric. This may be written as $V_i = V_G - V_T - V_{ch}(x)$, where $V_{ch}(x)$ is the potential along the channel. Using (32) for the electric field E_s and solving for the concentration of trapped electrons at the interface $n_t(\psi = \psi_s)$ we have

$$n_t(\psi = \psi_s) = \frac{C_i^2 (V_G - V_T - V_{ch})^2}{q\varepsilon\alpha V_{th}}. \tag{33}$$

The drain-source current $I_{\rm DS}$ can then be written as

$$I_{\rm DS} = W \frac{dV_{ch}}{dx} \int_0^{t_{\rm Si}} \sigma_n \left(V_{ch}(x), y\right) dy \tag{34}$$

where x denotes the location along the channel, and $t_{\rm Si}$ the a-Si:H layer thickness. Using (9) and (10) in (34), and changing the integral parameter from y to n_t yields

$$I_{\rm DS} = \frac{1}{2} W \frac{dV_{ch}}{dx} \int_{n_t(\psi=0)}^{n_t(\psi=\psi_s)} \sqrt{q\varepsilon\alpha V_{th}}\, \mu_{\rm eff} \frac{n_t^{\frac{\alpha}{2}-\frac{3}{2}}}{N_0^{\frac{\alpha}{2}-1}} dn_{\rm t}. \tag{35}$$

Substituting (33) into the solution for (35) yields

$$I_{\rm DS} = W \frac{dV_{ch}}{dx} \frac{(q\varepsilon\alpha V_{th} N_0)^{1-\frac{\alpha}{2}}}{\alpha - 1} \times \mu_{\rm eff} C_i^{\alpha-1} \left(V_G - V_T - V_{ch}(x)\right)^{\alpha-1}. \tag{36}$$

Multiplying by dx and integrating over both sides of (36) from source to drain yields

$$I_{\rm DS} = \frac{\mu_{\rm eff}}{\alpha} \zeta C_i^{\alpha-1} \frac{W}{L_{\rm eff}} \left[(V_{\rm GS} - V_T)^{\alpha} - (V_{\rm GD} - V_T)^{\alpha}\right] \tag{37}$$

where

$$\zeta = \frac{(q\varepsilon\alpha V_{th} N_0)^{1-\frac{\alpha}{2}}}{\alpha - 1} = \frac{(4.1 \times 10^{-16}\alpha)^{1-\frac{\alpha}{2}}}{\alpha - 1} \tag{38}$$

for a reference electron concentration, $N_0 = 10^{17}$ cm^{-3}. As a result, the parameter ζ with units $(\mathrm{C/cm}^2)^{\alpha-2}$ is only dependent on α and provides unit matching in the equation.

References

[1] P. Servati, S. Prakash, A. Nathan, and Ch. Py, "Amorphous silicon driver circuits for OLED displays," *J. Vac. Sci. Technol. A*, vol. 20, no. 4, pp. 1374–1378, Jul/Aug 2002.

[2] K. S. Karim and A. Nathan, "Readout circuit in active pixel sensors in amorphous silicon technology," *IEEE Electron Device Lett.*, vol. 22, pp. 469–471, Oct. 2001.

[3] M. Shur and M. Hack, "Physics of amorphous silicon based alloy field-effect transistors," *J. Appl. Phys.*, vol. 55, no. 10, pp. 3831–3842, 1984.

[4] M. S. Shur, H. C. Slade, M. D. Jacunski, A. A. Owusu, and T. Ytterdal, "SPICE models for amorphous silicon and polysilicon thin film transistors," *J. Electrochem. Soc.*, vol. 144, no. 8, pp. 2833–2839, 1997.

[5] M. Shur, M. Hack, and J. G. Shaw, "A new analytic model for amorphous silicon thin-film transistors," *J. Appl. Phys.*, vol. 66, no. 7, pp. 3371–3380, 1989.

[6] T. Leroux, "Static and dynamic analysis of amorphous-silicon field-effect transistors," *Solid State Electron.*, vol. 29, no. 1, pp. 47–58, 1986.

[7] K. Khakzar and E. H. Lueder, "Modeling of amorphous-silicon thin-film transistors for circuit simulations with SPICE," *IEEE Trans. Electron Devices*, vol. 39, pp. 1428–1434, June 1992.

[8] S.-S. Chen and J. B. Kuo, "An analytical a-Si:H TFT DC/capacitance model using an effective temperature approach for deriving a switching time model for an inverter circuit considering deep and tail states," *IEEE Trans. Electron Devices*, vol. 41, pp. 1169–1178, July 1994.

[9] P. Servati and A. Nathan, "Modeling of the static and dynamic behavior of a-Si:H TFTs," *J. Vac. Sci. Technol. A*, vol. 20, no. 3, pp. 1038–1042, 2002.

[10] B. Iñiguez, T. A. Fjeldly, and M. S. Shur, "Thin-film transistor modeling," *Int. J. High-Speed Electron. Syst.*, vol. 9, no. 3, pp. 703–723, 1999.

[11] D. Dosev, T. Ytterdal, J. Pallares, L. F. Marsal, and B. Iñíguez, "DC SPICE model for nanocrystalline and microcrystalline silicon TFTs," *IEEE Trans. Electron Devices*, vol. 49, pp. 1979–1984, Nov. 2002.

[12] S. Kishida, Y. Naruke, Y. Uchida, and M. Matsumura, "Theoretical analysis of amorphous-silicon field-effect-transistors," *Jpn. J. Appl. Phys.*, vol. 22, no. 3, pp. 511–517, 1983.

[13] L. Colalongo, "A new analytical model for amorphous-silicon thin-film transistors including tail and deep states," *Solid-State Electron.*, vol. 45, no. 9, pp. 1525–1530, 2001.

[14] C.-Y. Chen and J. Kanicki, "Origin of series resistances in a-Si:H TFTs," *Solid-State Electron.*, vol. 42, no. 5, pp. 705–713, 1998.
[15] A. Cerdeira, M. Estrada, R. García, A. Ortiz-Conde, and F. J. García Sánchez, "New procedure for the extraction of basic a-Si:H TFT model parameters in the linear and saturation regions," *Solid-State Electron.*, vol. 45, pp. 1077–1080, 2001.
[16] N. F. Mott and E. A. Davis, *Electronic Processes in Non-Crystalline Materials*. Oxford, U.K.: Clarendon, 1971.
[17] R. A. Street, *Hydrogenated Amorphous Silicon*. Cambridge, U.K.: Cambridge Univ. Press, 1991.
[18] J. G. Shaw and M. Hack, "An analytical model for calculating trapped charge in amorphous silicon," *J. Appl. Phys.*, vol. 64, no. 9, pp. 4562–4566, 1988.
[19] D. K. Schroder, *Semiconductor Material and Device Characterization*, 2nd ed. New York: Wiley, 1998.
[20] A. M. Miri and S. G. Chamberlain, "A totally wet etch fabrication technology for amorphous silicon thin film transistors," in *Proc. Mater. Res. Soc. Symp.*, vol. 377, 1995, pp. 737–742.
[21] D. Striakhilev, A. Sazonov, and A. Nathan, "Amorphous silicon nitride deposited at 120°C for OLED-TFT arrays on plastic substrates," *J. Vac. Sci. Technol. A*, vol. 20, no. 4, pp. 1087–1090, 2002.
[22] C. C. McAndrew and P. A. Layman, "MOSFET effective channel length, threshold voltage, and series resistance determination by robust optimization," *IEEE Trans. Electron Devices*, vol. 39, pp. 2298–2311, Oct. 1992.
[23] P. Servati, D. Striakhilev, and A. Nathan, "Above-threshold parameter extraction including contact resistance effects for a-Si:H TFTs on glass and plastic," in *Proc. Mat. Res. Soc. Symp.*, vol. 377, 2003, to be published.
[24] K. K. Ng and J. R. Brews, "Measuring the effective channel length of MOSFETs," *IEEE Circuits Devices Mag.*, vol. 6, pp. 33–38, 1990.
[25] K. Terada and H. Muta, "A new method to determine effective MOSFET channel length," *Jpn. J. Appl. Phys.*, vol. 18, no. 5, p. 953, 1979.
[26] J. G. J. Chern, P. Chang, R. F. Motta, and N. Godinho, "A new method to determine MOSFET channel length," *IEEE Electron Device Lett.*, vol. EDL-1, p. 170, Sept. 1980.
[27] J. Kanicki, F. R. Libsch, J. Griffith, and R. Polastre, "Performance of thin hydrogenated amorphous silicon thin-film transistors," *J. Appl. Phys.*, vol. 69, no. 4, pp. 2339–2345, 1991.
[28] D. J. Mountain, "Application of electrical effective channel length and external resistance measurement techniques to a submicrometer CMOS process," *IEEE Trans. Electron Devices*, vol. 36, pp. 2499–2505, Nov. 1999.

Peyman Servati (S'00) received the B.Sc. degree (with honors) in electronics engineering from the University of Tehran, Tehran, Iran, in 1998, and the M.A.Sc. degree from the University of Waterloo, Waterloo, ON, Canada, in 2000, where he is currently pursuing the Ph.D. degree, working on mechanically flexible TFTs and circuits for large area display and imaging applications.

As an undergraduate student, he was involved in electronic device simulation in the thin-film laboratories at the University of Tehran. Subsequently, he joined the a-SiDIC group of the University of Waterloo, focusing on modeling and characterization of a-Si:H TFTs. His research interests also include physics and technology of organic materials and devices.

Mr. Servati was a recipient of the bronze medal in the XXV I.Ph.O. competitions held in Beijing, China, 1994, and currently holds the Natural Sciences and Engineering Research Council (NSERC) of Canada Postgraduate Scholarship.

Denis Striakhilev (M'03) received the Dipl.Eng. and Ph.D degrees in semiconductor physics from the Moscow Institute of Electronic Technology (Technical University), [MIET (TU)], Moscow, Russia, in 1991 and 1996, respectively.

From 1997 to 1998, he was a Visiting Scientist with the Department of Physics, University of Kaiserslautern, Kaiserlautern, Germany and was a holder of a DAAD research scholarship. Subsequently, he was a Research Fellow with the Department of Material Science, MIET (TU) and Assistant Professor at the Department of Physics, Yaroslavl State Pedagogical University, Yaroslavl, Russia. Since 2000, he has been with the Department of Electrical and Computer Engineering, University of Waterloo, Waterloo, ON, Canada. His present research is primarily related to thin-film devices for display and imaging applications including mechanically flexible electronic devices. He is the author/coauthor of more than 30 publications and two patents. During his Ph.D work, he studied structural, electrical, and optical properties of amorphous semiconductor alloys for photovoltaic applications.

Dr. Striakhilev is a member of the Materials Research Society and Society for Information Displays.

Arokia Nathan (S'84–M'88–SM'99) received the Ph.D. degree in electrical engineering from the University of Alberta, Edmonton, AB, Canada, in 1988, where he was engaged in research related to the physics and numerical modeling of semiconductor microsensors.

In 1987, he joined LSI Logic Corporation, Santa Clara, CA, where he worked on advanced multichip packaging techniques and related issues. Subsequently, he was with the Institute of Quantum Electronics, ETH Zürich, Switzerland. In 1989, he joined the Department of Electrical and Computer Engineering, University of Waterloo, Waterloo, ON, Canada, where he is currently a Professor. In 1995, he was a Visiting Professor with the Physical Electronics Laboratory, ETH Zürich. His present research interests lie in amorphous and polycrystalline silicon devices, circuits, and systems on rigid and mechanically flexible substrates for digital imaging and displays. His interests have more recently encompassed polymer electronics, specifically on aspects related to the physics, technology, and applications of organic thin film transistors, displays, and sensors. He has published extensively in the field of sensor technology and CAD and is a coauthor of *Microtransducer CAD* (Berlin, Germany: Springer).

Dr. Nathan currently holds the DALSA/NSERC Industrial Research Chair in sensor technology and is a recipient of the Natural Sciences and Engineering Research Council E.W.R. Steacie Fellowship.